nature geoscience

ARTICLES

PUBLISHED ONLINE: 10 APRIL 2017 | DOI: 10.1038/NGEO2928

Experimental and observational evidence for plume-induced subduction on Venus

A. Davaille[1]*, S. E. Smrekar[2] and S. Tomlinson[3]

Why Venus lacks plate tectonics remains an unanswered question in terrestrial planet evolution. There is observational evidence for subduction—a requirement for plate tectonics—on Venus, but it is unclear why the features have characteristics of both mantle plumes and subduction zones. One explanation is that mantle plumes trigger subduction. Here we compare laboratory experiments of plume-induced subduction in a colloidal solution of nanoparticles to observations of proposed subduction sites on Venus. The experimental fluids are heated from below to produce upwelling plumes, which in turn produce tensile fractures in the lithosphere-like skin that forms on the upper surface. Plume material upwells through the fractures and spreads above the skin, analogous to volcanic flooding, and leads to bending and eventual subduction of the skin along arcuate segments. The segments are analogous to the semi-circular trenches seen at two proposed sites of plume-triggered subduction at Quetzalpetlatl and Artemis coronae. Other experimental deformation structures and subsurface density variations are also consistent with topography, radar and gravity data for Venus. Scaling analysis suggests that this regime with limited, plume-induced subduction is favoured by a hot lithosphere, such as that found on early Earth or present-day Venus.

Plate tectonics is responsible for the majority of Earth's heat loss, cycling of volatiles between the atmosphere and interior, and possibly even for maintaining habitability[1]. Despite its similarity in size and bulk density to Earth, Venus lacks plate tectonics, perhaps due to a dry interior[2] or high (460 °C) surface temperature[3,4]. However, many features on Venus are strikingly similar to terrestrial ocean–ocean subduction zones[5,6], although they also have characteristics of mantle plumes[6–8].

The initiation of subduction is not fully understood even on Earth. Numerous mechanisms have been proposed, including several related to mantle plumes. The edges of mantle plumes may be a favourable setting to initiate subduction. An example could be the Caribbean Plateau[9,10]. Lithospheric delamination above mantle upwellings can explain surface deformation in the Carpathian Mountains[11]. In the case of young oceanic or hot Venusian lithosphere, a very hot plume could reach the surface, breaking the lithosphere and initiating subduction by slab rollback[12,13]. However, these models require that the lithosphere becomes instantaneously very soft over a large area on top of the plume, which is problematic.

Most proposed subduction sites on Venus are located along arcuate trenches at the edges of the largest coronae. Coronae are volcanotectonic features unique to Venus. They were initially proposed to form via small-scale upwelling and subsequent relaxation due to their quasi-circular fracture pattern and central topography ranging from domes to plateaux to depressions[14]. Models of annular lithospheric delamination at the edges of an upwelling[15,16], downwelling[17], surface deformation due to pressure release melting[18], and plume-induced crustal convection[19] also produce many corona characteristics.

Conceptual attempts to reconcile subduction along outer trenches with an upwelling origin include foundering of the lithosphere due to: loading by crust thickened by pressure release melting above a plume[6,20]; thermal thinning above a plume head[6]; and weakening by extension over a plume[21,22]. The evidence for subduction was refuted on the basis of both evidence for plume upwelling and the apparent continuity of fractures across a subduction zone[23]. However, a set of faults continues across the Cascadia subduction zone off Oregon[24], indicating that this criterion alone cannot rule out subduction.

Laboratory experiments

One challenge for evaluating the plume-induced subduction mechanism is the difficulty of simulating the brittle elasto-visco-plastic, and history-dependent lithospheric rheology in three-dimensional (3D) numerical models, which still cannot fully model deformation on a wide range of scales. Laboratory experiments using complex rheology fluids provide a means to bridge this gap. The rheology of colloidal aqueous dispersions of silica nanoparticles depends strongly on the solid particle fraction, φ_p, deforming in the Newtonian regime at low φ_p, and transitioning to strain-rate weakening, plasticity, elasticity and brittle properties as φ_p increases[25]. Drying this system from above is analogous to cooling of a planetary mantle from above, as both rock cooling and solution desiccation are diffusion processes[26] (see Methods). As the colloidal solutions dry at constant humidity and temperature, a skin denser than the bulk fluid grows on the surface, akin to a planetary lithosphere. Under stress (for example, shear), this skin develops shear localization, but it can recover from damage with a healing time that depends on temperature and φ_p[25,27]. This is comparable to the memory displayed by polycrystalline damage zones in the lithosphere[4]. The instantaneous rheology of both the experimental skin and the lithosphere depends on their deformation history.

In the present experiments, the tank is dried from above and uniformly heated from below, allowing for the development of both a gravitationally unstable skin, the experimental 'lithosphere', and several hot upwelling plumes below this skin. Both processes are due to convection, either solutal or thermal, respectively. In both cases, the intensity of convection is in the range of a planetary mantle[28].

[1]Laboratoire FAST, CNRS/Univ. Paris-Sud/Université Paris-Saclay, 91405 Orsay, France. [2]Jet Propulsion Laboratory/Caltech, 4800 Oak Grove Drive, Pasadena, California 91109, USA. [3]Earth, Planetary, and Space Sciences, University of California Los Angeles, Los Angeles, California 90095, USA.
*e-mail: davaille@fast.u-psud.fr

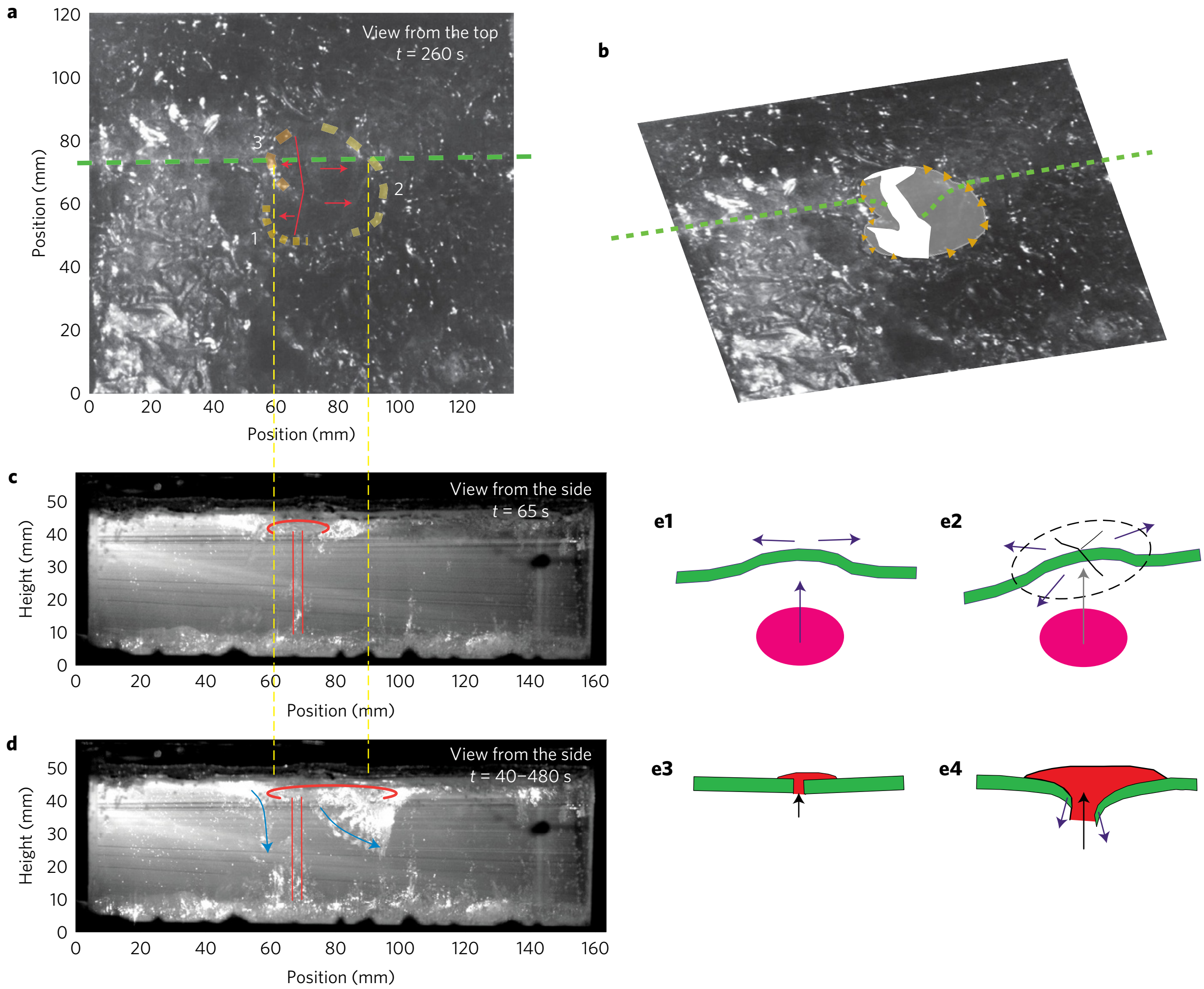

Figure 1 | Experiment in aqueous colloidal dispersion dried from above and heated from below. a–d, The side views (**c**,**d**) show a vertical laser cross-section indicated by the green line in the top views (**a**,**b**). The hot plume is indicated in red. Its impact under the surface results in three arcuate bulges (in yellow on **a**,**b**), and three associated subduction zones (in bright white on **c**,**d**). **a**, Top view 260 s after plume-induced subduction started. The initial fractures and the direction of plume spreading are indicated in red. **b**, The same as in **a** with an added sketch indicating the location and morphology of the subducting slabs, shown in grey. **c**, Side view at 65 s. Previously subducted slabs appear as brighter material at the bottom. **d**, Composite of 12 superposed images taken every 40 s starting at $t = 40$ s. The blue arrows show slab motion, including strong rollback on the right. **e**, Schematics showing the development of plume-induced subduction (see text).

The respective importance of elasticity, plasticity and memory on the system rheological and dynamical behaviour is also similar to the natural cases (see Methods).

Our experiments demonstrate the details of lithospheric deformation above a mantle plume (Fig. 1 and Supplementary Movie.). The skin flexes upwards above the rising plume[29,30] (Fig. 1e1), which puts it under tension[11,31]. Radial fractures and rifting of the skin then develop (Fig. 1e2), sometimes using pre-existing weaknesses (see Methods). Plume material upwells through the fractures because it is lighter than the skin and spreads as an axisymmetric gravity current above the broken denser skin (Fig. 1e3). This process represents a new, interesting mode of resurfacing (Fig. 1e4). The skin bends and sinks under the combined effects of its own weight and the plume gravity current[6,32] (Fig. 1e4).

A key observation is the formation of slab segments. Due to the brittle elasto-plastic behaviour of the lithosphere, the circular region above the plume cannot sink as a viscous sheet. Instead, the plate develops tears as a sheet of paper would do following intrusion[33] (Fig. 1b). Several slabs are therefore produced, localized along sections of the circular plume rim. Strong slab rollback is always observed (for example, slab on the right in Fig. 1d). Figure 1 shows three distinct slabs, a situation very different from the complete ring of cold downwelling obtained in purely viscous convection experiments[34,35]. In the experiment shown in Fig. 1, subduction stops when plume upwelling and spreading ceases. Slab pull is not strong enough to continue tearing the skin without further loading by plume material (see Methods). The subducted slab stays dangling until rehydrated (analogous to reheating in a planet) enough to allow viscous necking and detachment[36] to occur. The maximum length of a given slab is 20–80% of the surface plume head diameter (Fig. 1c). Numerous such episodes are observed in the experiment.

These experiments show that plume-induced subduction initially occurs when the lithosphere is in tension, a case favourable for planets since the lithosphere is weaker in tension than in compression[32,37]. Moreover, the characteristic dimensions of the areas affected by plume-induced subduction are those of a mantle plume head spreading on the surface. Given planetary mantle properties, this could reach 500 to 2,500 km diameter[29–31]. The duration of the whole process from subduction initiation to slab dangling would range between 20 and 200 Myr depending on asthenospheric viscosity, and slab characteristics mainly (see Supplementary Movie and Methods).

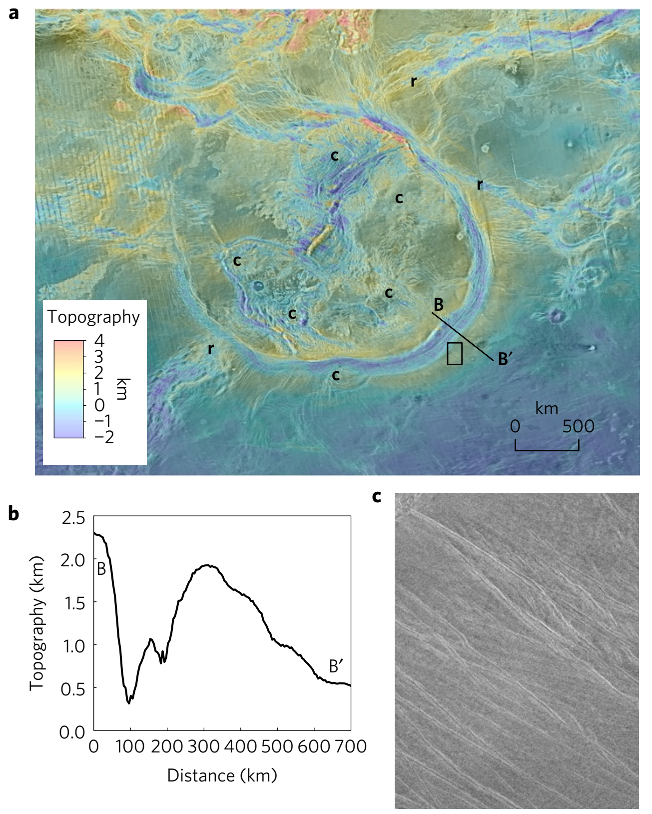

Figure 2 | Artemis Corona. a, Combined radar (greyscale) and topography (colour scale) image. The 300° segmented arc of fractures appears bright in the radar. The interior geology is complex, with intensely deformed linear, arcuate fracture zones, numerous volcanic flows, and 'corona-like' features[37] (labelled 'c'). Three rift segments (labelled 'r') radiate outward from the trench. **b**, Typical shape of the flexural bulge along line BB′ in **a**. **c**, 200-km-wide radar image (box in **a**) illustrating a pattern of bright–dark–bright lineaments indicative of graben on the outer topographic rise. They average 300 km in length and 1 km in width, with a spacing of 6–12 km.

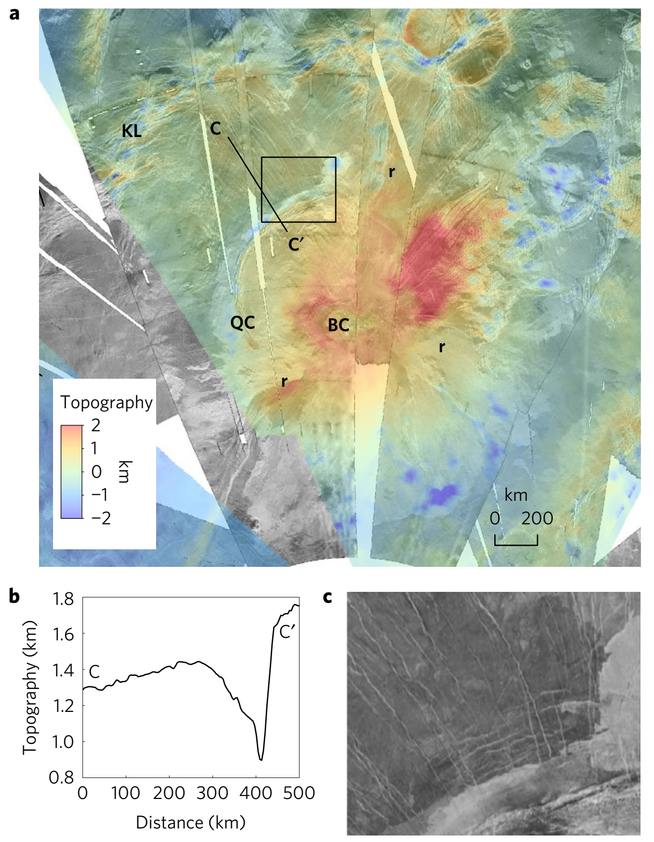

Figure 3 | Quetzalpetlatl Corona. a, A ~180° arc (labelled 'QC') of rough fractures appear radar bright (grey scale), located in a topographic trench (colour scale). Gaps indicate no data. The three exterior rift branches are labelled 'r', and Boala Corona 'BC'. **b**, Representative profile (black line CC′ in **a**) across the trench and outer rise. Voluminous volcanism partially fills the trench and may obscure its full extent to the south. **c**, Radar image (box in **a**) of graben and fractures occurring perpendicular to the trench with typical lengths of ~500 km, widths of 1 km, and ~10–25 km spacing.

Observational evidence of plume-induced subduction

On Venus, we suggest that Artemis and Quetzalpetlatl coronae are examples of plume-induced subduction. They have been interpreted as sites of mantle upwelling on the basis of their circular planform, their inner triple-junction-like rifts, volcanism, and gravity anomalies[38,39]. They also have large trenches and outer rises with evidence of bending and underthrusting[20,40] that have been interpreted as subduction zones[5,6,21]. As observed in the laboratory, both coronae have trenches only along an arcuate segment of their outer edge (Figs 2 and 3). In addition, they present narrow, more widely spaced grabens that originate at the trench and extend outward for hundreds of kilometres (Figs 2c and 3c). We interpret these grabens as a result of stretching of the outer bulge perpendicular to the direction of motion of a subducting plate as it is pulled down along an arcuate trench (as predicted theoretically[41]). This deformation of the lithosphere exterior to the trench is also observed in the experiment (Fig. 4).

The interior of Artemis is tectonically complex, with 5 small coronae or coronae-like features[38], and linear tectonic zones (Fig. 2). The latter have been interpreted as rift zones[38] and are similar to the multiple segments of rifting that are initially observed in the experiments (Fig. 1a). Moreover, Fig. 4 also shows circular surface deformation features that were created by small-scale convection under the newly formed lithosphere. These features, which are proportionally similar in scale to the corona-like features at Artemis, suggest a solution to the puzzle of how small-scale coronae could form within the larger scale corona.

Quetzalpetlatl Corona is distinguished by its prodigious volume of possibly recent volcanism. Some flows extend to the south for 1,500 km (Fig. 3) and have an estimated volume similar to that of the Deccan traps[42]. The surface thermal emissivity is anomalously high over this huge flow field, which could indicate either a very mafic composition, or relatively unweathered[39,43] and therefore geologically recent flows[44]. Like Artemis, Quetzalpetlatl has an arcuate trench segment, extensional fractures perpendicular to the trench, three rift branches extending outward from its rim, and an interior corona (Fig. 3).

Gravity data provide insights on subsurface structure and thus the likelihood of subduction. The large positive gravity anomalies associated with larger proposed subduction zones on Venus share many of the characteristics of terrestrial subduction zones[45]. The Bouguer gravity, which has the gravitational attraction of the topography removed (see Fig. 5 and Supplementary Methods C), reveals subsurface density variations. Quetzalpetlatl Corona has a large negative (−150 mGal) Bouguer anomaly (Fig. 5b), consistent with a low-density material such as a plume at depth. Near the trench, the Bouguer anomaly increases significantly, becoming positive just outside the trench. Artemis has a complex Bouguer gravity anomaly (Fig. 5a), with both strong positive values and negative values. Once the regional trend in topography and gravity has been removed (see Methods), the positive residual Bouguer

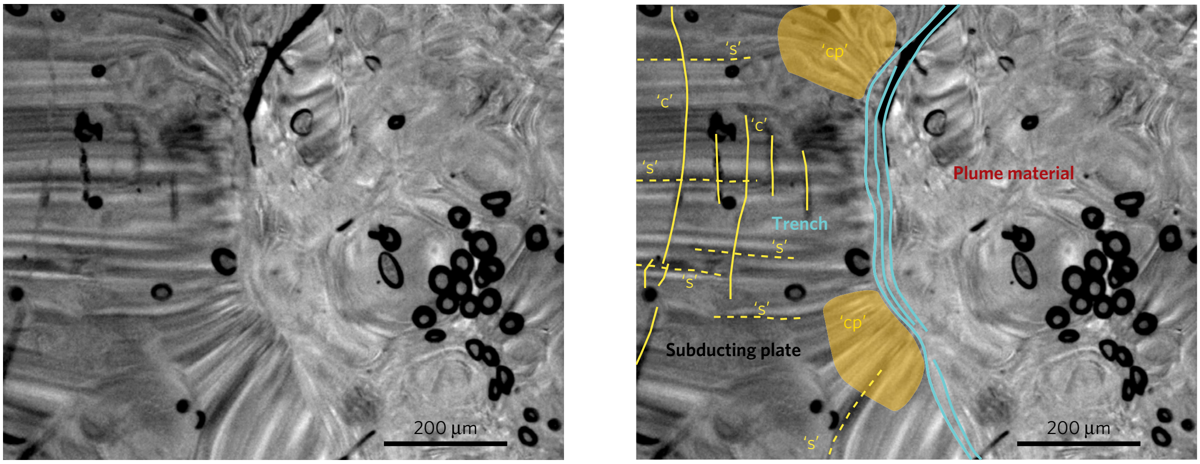

Figure 4 | Close up on the boundary between the subducting lithosphere and the plume material. The raw image (left; interpreted on the right) was taken 'post-mortem' in an experiment similar to Fig. 1: once the slab broke off, the remaining skin was scooped out of the tank and observed under a high-resolution camera from above. The skin is lit from below and reveals deformation features throughout. Darker areas correspond to thicker skin. The suture between the subducting skin and plume material is delineated by three lines (outlined in blue and by a (black) crack that occurred post-mortem). They represent the remnants of the trench, with highly faulted material due to the plastic deformation of the bending slab. Most of the subducting plate area shown corresponds to the flexural bulge. It shows the superposition of three types of deformation: cracks (yellow solid lines labelled 'c') parallel to the trench and mainly situated on the upper surface of the plate (they originate from extension perpendicular to the trench due to downward flexing of the lithosphere); compressive folds (orange zones labelled 'cp') on the bottom of the plate arriving perpendicular to the trench especially where the trench has the highest curvature; and striations on the top of the plate perpendicular to the trench and often hosting cracks (yellow dashed lines labelled 's'). These form as the flat plate stretches to accommodate subduction along the arcuate trench. In contrast, the plume side is less organized with several shear zones and small round or hexagonal structures due to small-scale convection (that is, downwellings) developing underneath the thickening new skin. The tiny round black features are (spurious) bubbles brought to the surface by the hot plume.

values occur in zones interpreted as rifts and could indicate significant thinning of the crust to bring higher density mantle material closer to the surface. The residual Bouguer anomaly is negative inside the trench and positive exterior to the trench.

We use a simple model of a slab at depth to assess the likelihood of subduction (see Methods). We fix the crustal and thermal density contrasts, and allow the crustal and thermal lithospheric thicknesses, and slab lengths and dips to vary. On the basis of our laboratory experiments, the slab length should be 20–80% of the corona diameter, and the slab dip (defined on Supplementary Fig. 2a) could reach 90°. Although the Bouguer gravity anomalies across the trenches at the two coronae are distinctly different, both can be fitted well by a slab at depth (Supplementary Fig. 2). The best fitting models (r.m.s. < 10 mGal) all have a crustal thickness of 10 km. The best fits at Quetzalpetlatl Corona are obtained for a lithospheric thickness of 125–150 km, a slab length of 250–750 km and a slab dip of 30°–90°. Although models with a slab dip of 30° have an r.m.s. < 10 mGal, steeper angles reproduce the shape of the Bouguer gravity better (Supplementary Fig. 2c). The best-fit ranges at Artemis coronae for lithospheric thickness are 75–100 km, 500–2,000 km for slab length and 60°–90° for dip (Supplementary Fig. 2b). Steeper dips and longer slabs provide a better fit to the more negative Bouguer anomaly. These longer slabs are consistent with the distance to apparent rift zones near the centre of Artemis.

We interpret the negative Bouguer gravity anomaly over the trench at Artemis and the resulting thinner lithosphere as compared with Quetzalpetlatl as indicating a warmer lithosphere that has partially equilibrated with the mantle. If the lithosphere at Artemis and Quetzalpetlatl had the same initial thickness when subducted, a 25 to 45 Myr time-lag between the two subduction events is sufficient to produce the present-day difference in their thermal thicknesses inferred from our analysis (see Supplementary Methods and Supplementary Fig. 3). Although this model is an oversimplification of a dynamic process and the allowable parameter range is large, the model fits are consistent with the presence of a subducted slab with the dips and dimensions seen in laboratory experiments.

We also examined the geoid and topography signatures of the coronae (see Methods). An isostatically compensated topographic feature will produce a cluster of points about a line on a plot of geoid versus topography; the slope is the geoid-to-topography ratio (GTR). As seen in Fig. 5c,d, there are multiple trends at each corona, each of which corresponds to a region with a distinct geologic signature and Bouguer anomaly (Fig. 5a,b). At Quetzalpetlatl, the GTR for the entire topographic high is intermediate (12.9 ± 7.1 m km^{-1}) between the Bouguer low that begins at Boala Corona and extends to the northeast (7.3 ± 4.4 m km^{-1}) and the region of the trench (19.5 ± 5.6 m km^{-1}). At Artemis, we find GTRs of 1.3 ± 0.2, 2.4 ± 7.0, 11.5 ± 7.2, and 31.4 ± 11.6 m km^{-1} for the northwestern fracture zone, the central rift/corona, the whole corona, and the trench area, respectively. GTR errors are relatively large due to poor gravity data resolution relative to the size of the subregions as well as the variety of geologic processes present.

Despite the difference in sign of the Bouguer anomalies between the two corona trench regions, the trench areas both have very large GTRs indicating deep compensation that is consistent with the presence of a slab. Interpreting the trench GTRs of 19.5 ± 5.6 and 31.4 ± 11.6 m km^{-1} as simple isostatic compensation gives a depth of several hundred kilometres. However, if there were both a hot plume and a cold slab, the apparent slab depth would be underestimated. Further, the topography is very likely to be at least partially elastically and dynamically supported, implying much larger compensation depths.

These results provide strong evidence for subduction. Laboratory experiments predict the asymmetric, arcuate trenches, and the extensional fractures that radiate outward from the trench, observed at Artemis and Quetzalpetlatl coronae, as well as at other coronae on Venus. The gravity data are also consistent with the thickness, lengths and dips of those observed in experiments. The presence of high emissivity flows at Quetzalpetlatl and the evidence for

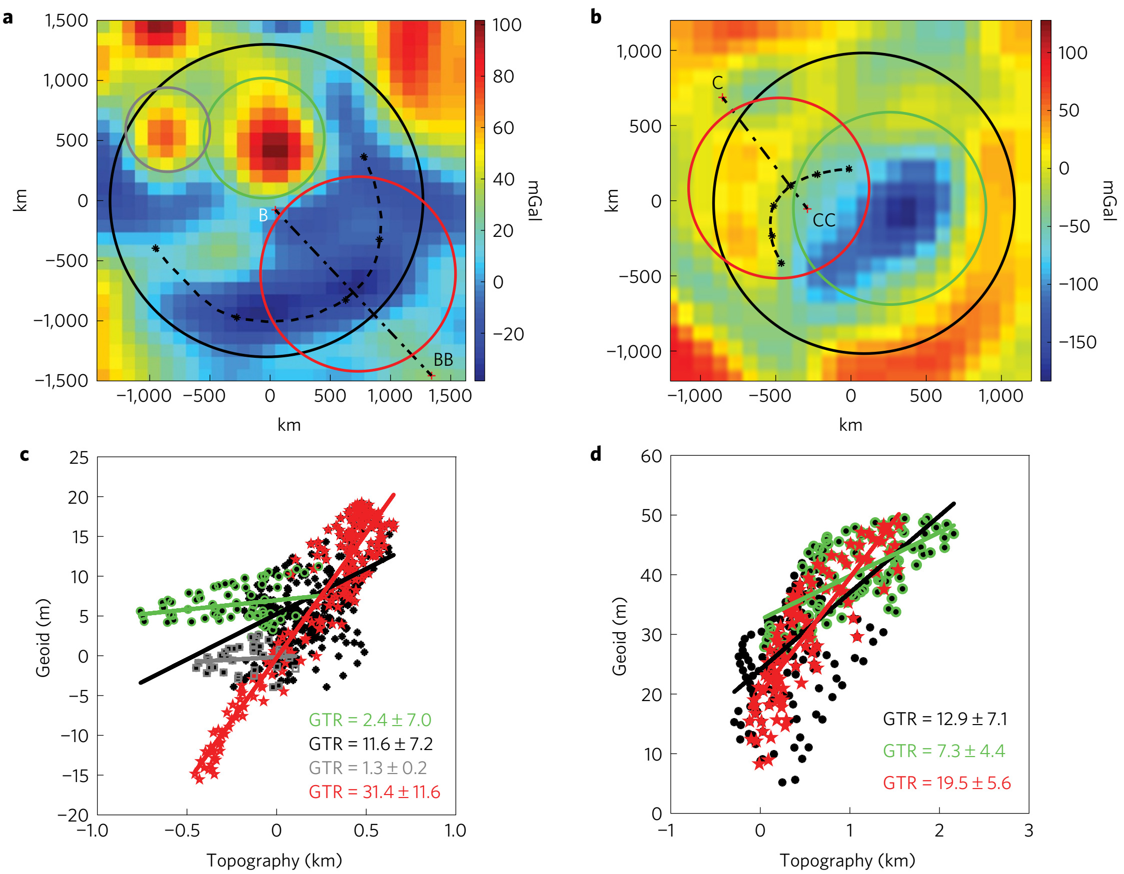

Figure 5 | Gravity data for Artemis and Quetzalpetlatl Coronae. a,b, Bouguer gravity (gravitational attraction of the topography has been removed) for the same regions as in Figs 2 and 3, indicating subsurface density variations at Artemis (**a**) and Quetzalpetlatl (**b**) coronae. The dashed lines indicate the trench location. The dot-dashed lines indicate the location of the Bouguer gravity profiles shown in Supplementary Fig. 2. **c**,**d**, GTRs calculated for the areas delimited by the corresponding coloured circles in **a** and **b**, respectively. Red areas enclose the trenches; green areas are rifts or plumes. Larger slopes imply greater compensation depths.

plumes at depth from gravity and topography data suggest that subduction is occurring at present. Artemis may be in a later stage of evolution. The multiple corona-like features may indicate small-scale convection in a cooling lithosphere, and the negative Bouguer anomaly above the trench also suggests that the slab has thermally equilibrated.

Present-day Venus dynamic regime

Venus appears therefore to be currently in a convective regime where subduction and lithosphere rejuvenation remain localized. In the experiments reported here, such events were not precursors of a complete rejuvenation of the experimental surface as was observed in numerical simulations[46,47]. Thus, this localized-subduction regime is not only different from plate tectonics (which implies continuous subduction and renewal of the surface), but also different from stagnant lid and episodic complete resurfacing, as had been proposed for Venus[22,46–48]. This new regime is more consistent with models that predict ongoing resurfacing of Venus[49,50].

The relative roles of volatiles and temperature in controlling Venusian lithospheric deformation remain unclear. However, scaling analysis checked against our experiments (see Methods) gives us a number of necessary conditions for plume-induced subduction as a function of the elasticity, strength, thickness of the lithosphere, plume characteristics and mantle temperature. This framework can help decipher differences between Venus and the Earth. For both planets, breaking the lithosphere with a large plume requires local plastic weakening of the lithosphere as already discussed. But rollback subduction will follow only if the extra load of plume material (a 5-km-thick volcanic load suddenly emplaced on top of the lithosphere would generate an extra stress around 150 MPa) is sufficient to bend rapidly the lithosphere. Figure 6 shows the subduction initiation domain based on this elasticity condition (KS > 1, see Methods) for a dry rheology[37] and an impinging plume 300 °C hotter than the mantle. For present-day Earth's mantle temperatures, plume-induced bending and subduction appears easier on Venus than on the Earth, due to the higher surface temperature of Venus, resulting in thinner elastic thickness. However, Fig. 6 also shows that the situation on present-day Venus is equivalent to the situation of Earth in the Archaean. This suggests that the hot lithosphere of Venus could be an analogue for early Earth, when conditions may have been favourable for the plume-induced subduction identified on Venus. Moreover, that subduction remains localized implies that the lithosphere has a short enough 'memory' so that no continuous plate boundaries can form. This is consistent with the hypothesis that the high temperatures on Venus, and on early Earth, may act to quickly heal the damage along shear zones[4]. The full range of our laboratory experiments show that for stronger and denser lithosphere, this same mechanism of plume-induced subduction can develop into an episode of complete resurfacing of the system, or into full-scale continuous plate tectonics.

A better understanding of melt-assisted rifting of the lithosphere and a better knowledge of Venus' overall lithospheric rheology and convective regime could constrain the requirements for the initiation of subduction and subsequent plate tectonics on Earth, as well as the likelihood of plate tectonics on rocky exoplanets.

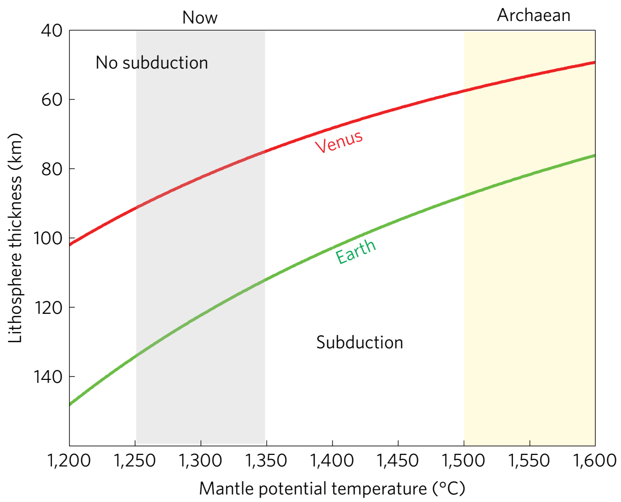

Figure 6 | Necessary condition for plume-induced subduction based on the elastic bending criterion (KS > 1) (see Methods). The lines represent KS = 1 for Venus (in red) and the Earth (in green). The plume is 300 °C hotter than the mantle and 100 kg m^{-3} less dense than the averaged lithosphere. For present-day mantle temperatures (grey area), plume-induced subduction is much easier on Venus than on the Earth. However, Archaean Earth (mantle temperature ∼200 °C higher, yellow area) appears quite similar to present-day Venus.

So far, we have been able to present detailed evidences of plume-induced subduction on only two sites on Venus, due to the paucity of high-resolution topography and gravity data. Higher-resolution imaging, topography, and gravity data for Venus would provide a better understanding of how Earth and its twin planet diverged down different geologic paths.

Methods

Methods, including statements of data availability and any associated accession codes and references, are available in the online version of this paper.

Received 9 December 2016; accepted 8 March 2017; published online 10 April 2017

References

1. Noack, L. *et al*. Can the interior structure influence the habitability of a rocky planet? *Planet. Space Sci.* **98,** 14–29 (2014).
2. Smrekar, S. E. *et al*. in *Exploring Venus as a Terrestrial Planet* (eds Esposito, L. W., Stofan, E. R. & Cravens, T. E.) 43–72 (AGU Geophysical Monograph 176, 2007).
3. Crameri, F. B. & Kaus, J. P. Parameters that control lithospheric—scale thermal localization on terrestrial planets. *Geophys. Res. Lett.* **37,** L09308 (2010).
4. Bercovici, D. & Ricard, Y. Plate tectonics, damage and inheritance. *Nature* **508,** 513–516 (2014).
5. McKenzie, D. *et al*. Features on Venus generated by plate boundary processes. *J. Geophys. Res.* **97,** 13533–13544 (1992).
6. Sandwell, D. T. & Schubert, G. Evidence for retrograde lithospheric subduction on Venus. *Science* **257,** 766–770 (1992).
7. Hansen, V. L. & Olive, A. Artemis, Venus: the largest tectonomagmatic feature in the solar system? *Geology* **38,** 467–470 (2010).
8. Sandwell, D. T. & Schubert, G. Flexural ridges, trenches, and outer rises around coronae on Venus. *J. Geophys Res.* **97,** 16069–16083 (1992).
9. Niu, Y., O'Hara, M. J. & Pearce, J. Initiation of subduction zones as a consequence of lateral compositional buoyancy contrast within the lithosphere: a petrological perspective. *J. Petrol.* **44,** 851–866 (2003).
10. Whattam, S. A. & Stern, R. J. Late Cretaceous plume-induced subduction initiation along the southern margin of the Caribbean and NW South America: the first documented example with implications for the onset of plate tectonics. *Gondwana Res.* **27,** 38–63 (2015).
11. Burov, E. & Cloetingh, S. Plume-like upper mantle instabilities drive subduction initiation. *Geophys. Res. Lett.* **37,** L03309 (2010).
12. Ueda, K., Gerya, T. & Sobolev, S. V. Subduction initiation by thermal–chemical plumes: numerical studies. *Phys. Earth Planet. Inter.* **171,** 296–312 (2008).
13. Gerya, T. V., Stern, R. J., Sobolev, S. V. & Whattam, S. A. Plate tectonics on the Earth triggered by plume-induced subduction initiation. *Nature* **527,** 221–225 (2015).
14. Stofan, E. R., Bindschadler, D. L., Head, J. W. & Parmentier, E. M. Coronae on Venus: models of origin. *J. Geophys. Res.* **96,** 20933–20946 (1991).
15. Smrekar, S. E. & Stofan, E. R. Coupled upwelling and delamination: a new mechanism for coronae formation and heat loss on Venus. *Science* **277,** 1289–1294 (1997).
16. Piskorz, D., Elkins-Tanton, L. T. & Smrekar, S. E. Coronae formation on Venus via extension and lithospheric instability. *J. Geophys. Res.* **119,** 2568–2582 (2015).
17. Hoogenboom, T. & Houseman, G. A. Rayleigh–Taylor instability as a mechanism for corona formation on Venus. *Icarus* **180,** 292–307 (2006).
18. Dombard, A. J., Johnson, C. L., Richards, M. A. & Solomon, S. C. A magmatic loading model for coronae on Venus. *J. Geophys. Res.* **112,** E04006 (2007).
19. Gerya, T. V. Plume-induced crustal convection: 3D thermomechanical model and implications for the origin of novae and coronae on Venus. *Earth Planet. Sci. Lett.* **391,** 183–192 (2014).
20. Brown, C. D. & Grimm, R. E. Tectonics of Artemis Chasma: a Venusian 'plate' boundary. *Icarus* **117,** 219–249 (1995).
21. Schubert, G. & Sandwell, D. T. A global survey of possible subduction sites on Venus. *Icarus* **117,** 173–196 (1995).
22. Fowler, A. C. & O-Brien, S. B. G. A mechanism for episodic subduction on Venus. *J. Geophys. Res.* **101,** 4755–4763 (1996).
23. Hansen, V. L. & Phillips, R. J. Tectonics and volcanism of Eastern Aphrodite Terra, Venus: no subduction no spreading. *Science* **260,** 526–530 (1993).
24. Goldfinger, C. *et al*. Transverse structural trends along the Oregon convergent margin: implications for Cascadia earthquake potential and crustal rotations. *Geology* **20,** 141–144 (1992).
25. Di Giuseppe, E., Davaille, A., Mittelstaedt, E. & François, M. Rheological and mechanical properties of silica colloids: from Newtonian liquid to brittle behavior. *Rheol. Acta* **51,** 451–465 (2012).
26. Müller, G. Starch columns: analog model for basalt columns. *J. Geophys. Res.* **103,** 15239–15253 (1998).
27. Amiri, A., Oye, G. & Sjöblom, J. Temperature and pressure effects on stability and gelation properties of silica suspensions. *Colloids Surf.* **378,** 14–21 (2011).
28. Schubert, G., Turcotte, D. L. & Olson, P. *Mantle Convection in the Earth and Planets* (Cambridge Univ. Press, 2001).
29. Olson, P. & Nam, I. S. Formation of seafloor swells by mantle plumes. *J. Geophys. Res.* **91,** 7181–7191 (1986).
30. Griffths, R. W., Gurnis, M. & Eitelberg, G. Holographic measurements of surface topography in laboratory models of mantle hotspots. *Geophys. J.* **96,** 1–19 (1989).
31. Koch, D. M. & Manga, M. Neutrally buoyant diapirs: a model for Venus coronae. *Geophys. Res. Lett.* **23,** 225–228 (1996).
32. Kemp, D. V. & Stevenson, D. J. A tensile, flexural model for the initiation of subduction. *Geophys. J. Int.* **125,** 73–94 (1996).
33. Vermorel, R., Vandenberghe, N. & Villermaux, E. Radial cracks in perforated thin sheets. *Phys. Rev. Lett.* **104,** 175502 (2010).
34. Olson, P., Schubert, G., Anderson, C. & Goldman, P. Plume formation and lithosphere erosion: a comparison of laboratory and numerical experiments. *J. Geophys. Res.* **93,** 15065–15084 (1988).
35. Androvandi, S., Davaille, A., Limare, A., Fouquier, A. & Marais, C. At least three scales of convection in a mantle with strongly temperature-dependent viscosity. *Phys. Earth Planet. Inter.* **188,** 132–141 (2011).
36. Schmalholz, S. M. A simple analytical solution for slab detachment. *Earth Planet. Sci. Lett.* **304,** 45–54 (2011).
37. Kohlstedt, D. L., Evans, B. & Mackwell, S. J. Strength of the lithosphere: constraints imposed by laboratory experiments. *J. Geophys. Res.* **100,** 17587–17602 (1995).
38. Hansen, V. L. Artemis: signature of a deep mantle plume on Venus. *Geol. Soc. Am. Bull.* **114,** 839–848 (2002).
39. Ivanov, M. & Head, J. W. Lada Terra rise and Quetzalpetlatl Corona: a region of long-lived mantle upwelling and recent volcanic activity on Venus. *Planet. Space Sci.* **58,** 1880–1894 (2010).
40. Brown, C. D. & Grimm, R. E. Lithospheric rheology and flexure at Artemis Chasma, Venus. *J. Geophys. Res.* **101,** 12697–12708 (1996).
41. Tanimoto, T. State of stress within a bending spherical shell and its implications for subducting lithosphere. *Geophys. J. Int.* **134,** 199–206 (1998).
42. Kratter, K. M., Carter, L. M. & Campbell, D. B. An expanded view of Lada Terra, Venus: new Arecibo radar observations of Quetzalpetlatl Corona and surrounding flows. *J. Geophys. Res.* **112,** E04008 (2007).

43. Helbert, J., Müller, N., Kostama, P., Piccioni, G. & Drossart, P. Surface brightness variations seen by VIRTIS on Venus Express and implications for the evolution of the Lada Terra region, Venus. *Geophys. Res. Lett.* **35,** L11201 (2008).
44. Smrekar, S. E. *et al*. Recent hotspot volcanism on Venus from VIRTIS emissivity data. *Science* **328,** 605–608 (2010).
45. Schubert, G., Moore, W. B. & Sandwell, D. T. Gravity over coronae and chasmata on Venus. *Icarus* **112,** 130–146 (1994).
46. Armann, M. & Tackley, P. J. Simulating the thermochemical magmatic and tectonic evolution of Venus's mantle and lithosphere: two-dimensional models. *J. Geophys. Res.* **117,** E12003 (2012).
47. Crameri, F. & Tackley, P. J. Subduction initiation from a stagnant lid and global overturn: new insights from numerical models with a free surface. *Prog. Earth Planet. Sci.* **3,** 30 (2016).
48. Moresi, L. & Solomatov, V. Mantle convection with a brittle lithosphere: thoughts on the global tectonic styles of Earth and Venus. *Geophys. J. Int.* **133,** 669–682 (1998).
49. Bjonnes, E. E., Hansen, V. L., James, B. & Swenson, J. B. Equilibrium resurfacing of Venus: results from new Monte Carlo modeling and implications for Venus surface histories. *Icarus* **217,** 451–461 (2012).
50. O'Rourke, J. G., Wolf, A. S. & Ehlmann, B. L. Venus: interpreting the spatial distribution of volcanically modified craters. *Geophys. Res. Lett.* **41,** 8252–8260 (2014).

Acknowledgements
Part of this research was carried out at the Jet Propulsion Laboratory, California Institute of Technology, under a contract with the National Aeronautics and Space Administration. S.E.S. was supported by Jet Propulsion Laboratory internal funds, and A.D. by grants from PNP-INSU and the French ANR 'PTECTO' (ANR-09-BLAN-0142). A.D. is grateful for the technical support of A. Aubertin, R. Pidoux and L. Auffray.

Author contributions
A.D. carried out the laboratory experiments, determined the scaling laws, and proposed the geodynamical model for Venus plume-induced subduction. S.E.S. chose Venusian analogue sites and analysed image data. S.T. analysed gravity and topography data. S.E.S. and A.D. wrote the manuscript.

Additional information
Supplementary information is available in the online version of the paper. Reprints and permissions information is available online at www.nature.com/reprints. Publisher's note: Springer Nature remains neutral with regard to jurisdictional claims in published maps and institutional affiliations. Correspondence and requests for materials should be addressed to A.D.

Competing financial interests
The authors declare no competing financial interests.

Methods

Laboratory experiments. The experiments reported here are part of a larger body using complex rheology fluids (to date, about 80 experiments using visco-plastic polymers and about 60 experiments using brittle visco-elasto-plastic thixotropic colloidal dispersions) to study the influence of rheology on the convective patterns. It is beyond the scope of this paper to describe all of the different regimes observed and here we focus only on the experiments that showed plume-induced subduction. We used Ludox TM50 silica colloidal dispersions from Sigma-Aldrich. A glass tank 150 × 150 × 50 mm was filled with the solution and placed in a climatic chamber, whereby the temperature (22–30 °C) and humidity (20–50%) above the fluid surface were kept uniform and constant. The bottom of the tank was uniformly heated from below at constant temperature ranging between 30 °C and 80 °C. The tank was on a scale to record the evolution of mass and evaporation rate. At $t = 0$, the fluid is homogeneous, with a particle volume fraction of 30%, and therefore Newtonian[25]. Both drying from above at a constant evaporation rate Evap (and constant temperature $T_{\rm cold}$) and heating from below at constant temperature $T_{\rm hot} = T_{\rm cold} + \Delta T$ are started at $t = 0$. The horizontal top surface as well as a vertical cross-section were illuminated with a green laser sheet (532 nm), and images were taken with two still cameras every 4 s to 5 min. Each experiment lasted between 3 days and 2 weeks.

Dimensionless numbers. The experiments were all conducted in the limit $\nu/\kappa_{\rm i} \gg 1$ relevant to the Earth[28], whereby momentum diffusivity, ν (kinematic viscosity of the bulk fluid), is much larger than $\kappa_{\rm i}$, the thermal diffusivity ($\kappa_{\rm t}$ for thermal convection) or the chemical diffusivity (of individual particles, $\kappa_{\rm c}$, for the drying process).

The thermal plume intensity is related to the thermal Rayleigh number, which compares the driving thermal buoyancy forces to the resisting effects of thermal diffusion and viscous dissipation:

$$\mathrm{Ra_t} = \frac{\alpha g \Delta T H^3}{\kappa_{\rm t} \nu}$$

where α is the thermal expansivity, H is the fluid thickness, and g is the gravity acceleration. In the experiments, $\mathrm{Ra_t}$ ranges between 10^6 and 10^9, so that hot plumes are expected to develop, as in a planetary mantle[28].

The gravitational instability of the skin is characterized by a solutal Rayleigh number, where the density contrast driving convection $\Delta\rho$ is due to heterogeneities in the particle volume fraction:

$$\mathrm{Ra_{ch}} = \frac{\Delta\rho g H^3}{\rho \kappa_{\rm c} \nu}$$

As the chemical diffusivity $\kappa_{\rm c}$ depends also on the particle volume fraction[51,52], here $\mathrm{Ra_{ch}}$ initially varies between 10^8 and 10^{11}.

Evaporation of water at the free top surface generates an accumulation of silica particles at the liquid–air interface and forms a visco-elasto-plastic skin if the characteristic timescale of evaporation $t_{\rm E} = H/\mathrm{Evap}$ is smaller than the chemical diffusion timescale $t_{\rm D} = H^2/\kappa_{\rm c}$. This defines the Peclet number $\mathrm{Pe} = \mathrm{Evap}\, H/\kappa_{\rm c}$, which ranged from 30 to 600 in our experiments, therefore ensuring skin formation. As shown in Supplementary Fig. 1, this skin thickens through time following a generalized diffusion equation[51,52] (A. Davaille, E. Di Giuseppe, G.-J. Michon & A. Aubertin, manuscript in preparation). As the density increases with the silica particle volume fraction[25], the skin becomes denser than the bulk fluid underneath and therefore more gravitationally unstable as time increases. From the particle volume fraction profiles of Supplementary Fig. 1 and the rheology measurements[25], we can calculate the variations of elastic modulus, yield stress (that is, limit of linear elasticity), and viscosity across the skin. LudoxTM50 visco-elasto-plastic properties develop for particle volume fraction $\phi \geq 0.40$ (ref. 25). Supplementary Fig. 1 shows that this occurs within less than 15 s of evaporation through the top free boundary.

The viscosity variations (measured by the viscosity ratio γ) span more than 6 orders of magnitude in a well-developed skin (Supplementary Fig. 1). Hence, if the fluid was purely viscous, it would remain in a stagnant lid regime whereby convection develops below a very viscous skin[53–55].

From the skin thickness $h_{\rm skin}$ and viscosity structure, we can also evaluate its effective flexural stiffness: $D_{\rm flex} = \gamma\left[\frac{h_{\rm skin}}{H}\right]^3$, which ranges between 0.1 and 30 in our experiments. According to Petersen *et al.*[56], for the range of $Ra_{\rm ch}$ in the laboratory ($>10^7$), those $D_{\rm flex}$ values put our experiments in the one-sided subduction regime, once subduction has started.

The Deborah number, $\mathrm{De} = (\eta_{\rm L}/E_{\rm Y})(U/l_{\rm B})$, represents the ratio of the characteristic timescale for visco-elastic stress relaxation ($\eta_{\rm L}/E_{\rm Y}$, where $\eta_{\rm L}$ is the viscosity of the lithosphere and $E_{\rm Y}$ is its Young modulus) to the characteristic timescale of deformation. Following Fourel *et al.*[57], we choose the latter as the time $l_{\rm B}/U$ a slab particle spends in the bending region of length $l_{\rm B}$ when it is sinking at the velocity $U \sim \Delta\rho g h_{\rm skin} l/\eta_{\rm m}$, where $\eta_{\rm m}$ is the mantle viscosity and l is the subducting slab length. The flexural bulge must be added to l to obtain the bending region length $l_{\rm B}$. For our experiments, $10^{-4} \leq \mathrm{De} \leq 0.15$. This is in the same range as a planetary lithosphere ($\mathrm{De} < 1$), which implies the importance of both viscous and elastic behaviour[58]. Since $l \leq l_{\rm B}$, $\mathrm{De_i} \geq \gamma(\Delta\rho g h_{\rm skin}/E_{\rm Y})$. When subduction starts in the experiment shown in the Supplementary Movie, $\mathrm{De_i} = 0.0785$, placing it at the edge of the elasticity-dominated regime according to Fourel *et al.*[57]. For a planet, $\mathrm{De_i} = \gamma \times 1.4 \times 10^{-3}$, placing it again in the elasticity-dominated regime as soon as $\gamma > 100$. It is therefore expected that elasticity would be important during subduction initiation.

The Bingham number, Bi, compares the yield stress $\sigma_{\rm Y}$ to the gravity force: $\mathrm{Bi} = \sigma_{\rm Y}/h_{\rm skin} g \Delta\rho$. According to Supplementary Fig. 1, this gives values between 10^2 and 10^6, so that gravitational instability of the skin alone would not be sufficient to rupture the skin. We are therefore running into the same problem as for a planetary lithosphere: on the basis of the instantaneous values of the rheology measured on small samples, the skin/lithosphere material is much too strong and viscous to develop subduction without an additional weakening mechanism.

Typical evolution during an experiment. As soon as fresh liquid suspension starts to evaporate, a skin forms within 15 s (Supplementary Fig. 1). As it thickens, buckling appears (Fig. 1a,b) with typical wavelength around 10 mm. This mechanical instability occurs because the skin becomes under contraction as particle concentration gradients develop when losing water[59]. The wavelength is coherent with scaling in visco-elastic fluids[58]. However, as the buckling amplitude increases, strain and stress increase, until the skin becomes partially yielded or very close to it along a number of zones. The upcoming plumes thus encounter a skin that contains long-lived shear zones, and is weaker than the calculated strength of the skin in Supplementary Fig. 1. Plumes are likely to initiate subduction, as described in the main text of this paper. Experiments run in the same drying conditions but without heating from below and hot plume generation also show subduction events, but they start much later (about a hour instead of 17 min), and involve a thicker and denser skin.

Necessary conditions for plume-induced subduction. A number of 'local' (in time and space) criteria have to be fulfilled to observe plume-induced subduction.

First of all, the lithosphere has to be gravitationally unstable, so it should be on average denser than the underlying mantle ($\rho_{\rm L} > \rho_{\rm m}$). This is always the case in our experiments. However, since the crust of a planet is lighter than the mantle, this condition puts tight constraints over the crustal and lithospheric thickness at the time of initiation since those two trade off (see the gravity section below for detailed calculations). For example, as the Earth's continental lithosphere is lighter than the mantle underneath due to its thick crust, a LIP erupting on a continent will never initiate subduction. Similarly, subduction would be inhibited if underplating of buoyant plume melt residuum is too voluminous.

Additionally, the lithosphere should be able to strongly localize deformation so that it can break. In a visco-plastic formulation, this implies that the deviatoric stress should locally exceed the lithosphere strength[47], $\sigma_{\rm dev} > \sigma_{\rm Y}$ (that is, $\mathrm{Bi} < 1$). Recent laboratory measurements on natural samples give maximum lithospheric strength around 300 to 500 MPa (refs 60,61). Numerical simulations then show that instantaneous stresses arising from thermal convection alone are not sufficient to overcome those values[46,62]. Hence, one has to consider additional processes: to increase the local deviatoric stress; or/and to decrease the lithosphere strength. For the latter, shear-heating coupled to buckling can be important[3]; long-time development of damage zones due to polycrystal dynamics[4], contraction cracks in the oceanic lithosphere[63], and weak layer interconnection[64] have also been invoked. In the case of a hot plume impinging under the lithosphere, volcanism and diking certainly contribute to weakening the lithosphere prior to subduction[12,13]. If one supposes that the whole lithospheric area above the plume is suddenly weakened, subduction develops first as a viscous ring[13]. If weakening is more localized on radial faults (as in our experiments), subduction will develop in segments between these faults. Another important consideration is that the lithospheric strength in extension is half that of the lithospheric strength in compression[65]. A rising plume of radius $R_{\rm P}$ and density anomaly $\Delta\rho_{\rm P} = \rho_{\rm P} - \rho_{\rm L}$ puts the lithosphere in extension, producing a peak deviatoric stress $\sigma_{\rm dev} = 0.2 g \Delta\rho_{\rm P} R_{\rm P}$, reaching 100–470 MPa for ($R_{\rm P}$, $\Delta\rho_{\rm P}$) ranging between (500 km, 100 kg m^{-3}) and (600 km, 400 kg m^{-3}), respectively[31]. Failure of the lithosphere would therefore be more likely for the largest plumes, and would probably require an additional mechanism to soften the lithosphere as well, as discussed above.

Once the lithosphere has failed, subduction proceeds only if the hot plume material can flood the lithosphere, and if the lithosphere can bend rapidly enough compared with the cooling time of the plume material. When subduction starts, the lithosphere bends under the loading of the hotter and less dense plume material gravity current spreading at the surface (Fig. 1e). On a planet, there would be an initial volcanic loading stage, followed by exposure of mantle plume material as subduction proceeds. If the length of the lithospheric failure is much larger than the lithosphere thickness (as seen in the laboratory), we can use as a first approximation the 2D elastic flexural analysis of Kemp and Stevenson[32]. Then subduction proceeds if

$$\mathrm{KS} = \frac{16}{9}\frac{\Delta\rho_{\mathrm{P}} g h_{\mathrm{skin}}^3}{\kappa \eta_{\mathrm{P}}}\left(\frac{\Delta\rho_{\mathrm{P}}}{\rho_{\mathrm{m}}}\right)^4\left(\frac{3\rho_{\mathrm{m}} g(1-\nu_{\mathrm{P}}^2)h_{\mathrm{skin}}}{E_{\mathrm{Y}}}\right)^{1/2}\left(\frac{T_{\mathrm{m}}-T_{\mathrm{surf}}}{T_{\mathrm{e}}-T_{\mathrm{surf}}}\right)^{3/2}$$

is greater than a critical value $\mathrm{KS_c}=1$, where η_{P} is the viscosity of the hot plume material, E_{Y} is the elastic modulus, ν_{P} is the Poisson ratio and T_{e} is the isotherm below which the plate is elastic. The thickness of the elastic part of the plate for a planet would scale as $h_{\mathrm{skin}}(T_{\mathrm{m}}-T_{\mathrm{surf}})/(T_{\mathrm{e}}-T_{\mathrm{surf}})$.

Our experiments showed that plume-induced subduction was able to start when we had locally $\mathrm{KS_c} \geq 1.1 \pm 0.2$, where the uncertainty is due to the physical properties. We shall therefore take the same $\mathrm{KS_c}=1$ as Kemp and Stevenson[32] when applying this criterion to Venus and the Earth (Fig. 6). The calculations were done with $g = 9.81\ \mathrm{m\,s^{-2}}$ for the Earth and $g = 8.87\ \mathrm{m\,s^{-2}}$ for Venus; T_{surf} (Venus) $= 460\,^{\circ}\mathrm{C}$ and T_{surf} (Earth) $= 0\,^{\circ}\mathrm{C}$, $E_{\mathrm{Y}} = 70$ GPa, $\nu_{\mathrm{P}} = 0.3$, $\kappa = 10^{-6}\ \mathrm{m^2\,s^{-1}}$; $T_{\mathrm{e}} = 650\,^{\circ}\mathrm{C}$, and a dry rheology[37]. This choice is a 'worst-case' scenario, as it is still debated whether Venus interior is as dry as its surface. By lowering the viscosity in KS, a wet rheology would be even more favourable.

Duration and fate of plume-induced subduction. Once subduction has been initiated, time can be scaled with the characteristic timescale of a slab sinking under its own weight $t_{\mathrm{N}} = \eta_{\mathrm{m}}/(h_{\mathrm{skin}}\, g\, \Delta\rho)$ (ref. 66). We can therefore use this timescale to convert the times in the laboratory experiments to Venusian times (see Supplementary Movie). It shows that the whole process from the initiation to the arrest of subduction could take between 20 and 200 Myr, for an asthenospheric viscosity ranging from 10^{19} to 10^{20} Pa s^{-1} (refs 2,46). These estimates do not take into account the increase in averaged slab density that could result from the transformation of lighter crust in denser eclogite at depth, nor the fact that at first, the slab would sink into the less viscous plume material. Both processes would increase the sinking velocity and therefore reduce the time estimates.

In our plume-induced experiments, subduction proceeded mostly through rollback, and completely stopped when plume upwelling and spreading ceased. This is different from the 2D cases[12], where subduction either continued until reaching the computational domain edges, or stopped because of slab viscous necking and detachment (this second case occurred with weak slabs). Viscous necking and slab cutoff also eventually occurred in our experiments, but much later than the arrest of subduction (see Supplementary Movie). Our experiments are 3D, and therefore, rollback subduction can continue only if the lithosphere continues to tear along the slab edges, which requires energy. On Earth, this is the well-known problem of the STEP (Subduction-Transform Edge Propagator) faults at the edges of subduction zones[67] and tear resistance at the edge of a slab has been found to be an important parameter controlling the evolution of subduction zones. Recent 3D numerical studies have shown that slab rollback requires quite low yield strength (<25–50 MPa) along the tear fault and will become arrested for values greater than 100 MPa (ref. 68); so that slab edges tend to tear preferentially along pre-existing sutures if present[69]. This highlights again the importance of long-term storage of large-scale weak/shear zones in the lithosphere for the development of long-term subduction[4,64,70].

Bouguer gravity analysis and slab models. For each region, the gravitational attraction due to topography assuming a basaltic crust (2,900 kg m^{-3}) is subtracted from the free-air gravity data to calculate the Bouguer gravity, thus revealing subsurface density variations. At Artemis, the gravity and topography are strongly influenced by the large topographic plateau to the north, Aphrodite Terra. Thus, we first remove the regional trend by fitting a plane to the free-air gravity, geoid and topography separately. The offsets across the best-fit gravity and topography planes are approximately 80 mGal and 1.7 km, respectively. These regional trends are subtracted from the free-air gravity and topography before analysing the data. If the regional trend is not removed, the shape of the Bouguer gravity profile is similar but tens of milligals more negative. At Quetzalpetlatl, there is no regional trend. However, there are other geologic features in the vicinity of the trench that are likely to influence the gravity and topography. In the fits in Supplementary Fig. 2c, 30 mGal has been added to the Bouguer gravity. This overall negative Bouguer gravity signature at Quetzalpetlatl is likely to be due to the presence of a plume at depth. This is done to accommodate the model fits, which go to 0 away from the slab (see Supplementary Fig 2a). If no offset is introduced into the data, the same models are preferred but the r.m.s. values increase by ∼10 mGal.

Model fits for different Bouguer profile lengths were considered. The best fits cover the regions that extend outward to the point where other geologic features are evident in the radar imaging and in the gravity data. In the interior of Artemis, the Bouguer gravity becomes positive near the linear fracture zone, implying relatively high density material at depth. This high density could be due to delamination of the crust and lithosphere, as seen in laboratory experiments. Alternatively, the fracture zone interpreted as a rift may have thinned the crust, bringing the mantle closer to the surface. At Quetzalpetlatl, there is a fracture zone at approximately 500 km out board of the trench near the Bouguer gravity low. There is also a strong positive Bouguer gravity anomaly ∼1,000 km from the trench, where a ridge and fracture belt occurs. In the interior, the Bouguer gravity becomes strongly negative, consistent with the presence of a hot mantle plume.

We compare a simple, 2D model[71] of the gravitational attraction of a cold subducting lithosphere with an embedded basaltic crust to a profile of the Bouguer gravity across the trench. The crustal and mantle densities are based on terrestrial basalt and olivine densities of 2,900 and 3,300 kg m^{-3}, respectively, giving $\Delta\rho_{\mathrm{c}} = 400\ \mathrm{kg\,m^{-3}}$. The average thermal density contrast due to the cold lithosphere subducting into the mantle is $\Delta\rho_{\mathrm{L}} = \rho\alpha\Delta T/2 \cong 30\ \mathrm{kg\,m^{-3}}$, where $\alpha = 2.4\times10^{-5}\ \mathrm{K^{-1}}$ and ΔT is the mean temperature difference across the lithosphere, based on the surface temperature of 460 °C and an assumed mantle temperature of 1,300 °C. This model yields either a negative or positive gravity anomaly based on the slab length and thickness of the crust and lithosphere. Crustal thickness, Z_{C}, and thermal lithospheric thickness, Z_{L}, range from 10 to 50 km (10 km increments) and 50 to 200 km (25 km increments), respectively. These ranges are based on estimates of these parameters in the literature derived from gravity and topography data[72–74]. On the basis of the slabs observed in the laboratory (Fig. 1), we examine subduction angles, β, of 30°, 60° and 90°, and plate lengths of ∼20–80% of the corona diameter, corresponding to 500 to 2,000 km for Artemis and 250 to 1,000 km for Quetzalpetlatl, in increments of 250 km. If the slab dip is as large as seen in the laboratory (up to 90°), much of the gravity anomaly will be centred near the topographic bulge. Models are calculated at the resolution of the gravity data at each corona (∼400 km at Artemis and ∼300 km at Quetzalpetlatl) using a running average of the output model points.

Data availability. The data that support the findings of this study are available from the corresponding author on request.

References

51. Brown, L. A., Zukoski, C. F. & White, L. R. Consolidation during drying of aggregated suspensions. *AIChE J.* **48,** 492–502 (2002).
52. Style, R. W. & Peppin, S. S. L. Crust formation in drying colloidal suspensions. *Proc. R. Soc. A* **467,** 174–193 (2011).
53. Morris, S. & Canright, D. R. A boundary-layer analysis of Benard convection with strongly temperature-dependent viscosity. *Phys. Earth Planet. Inter.* **36,** 355–373 (1984).
54. Davaille, A. & Jaupart, C. Transient high-Rayleigh number thermal convection with large viscosity variations. *J. Fluid Mech.* **253,** 141–166 (1993).
55. Solomatov, S. Scaling of temperature- and stress-dependent viscosity convection. *Phys. Fluids* **7,** 266–274 (1995).
56. Petersen, R. I., Stegman, D. R. & Tackley, P. J. A regime diagram of mobile lid convection with plate-like behavior. *Phys. Earth Planet. Inter.* **241,** 65–76 (2015).
57. Fourel, L., Goes, S. & Morra, G. The role of elasticity in slab bending. *Geochem. Geophys. Geosyst.* **15,** 4507–4525 (2014).
58. Schmalholz, S. M. & Podladchikov, Y. Buckling versus Foldin: importance of viscoelasticity. *Geophys. Res. Lett.* **26,** 2641–2644 (1999).
59. Boulogne, F., Giorgutti-Dauphiné, F. & Pauchard, L. The buckling and invagination process during consolidation of colloidal droplets. *Soft Matter* **9,** 750–757 (2014).
60. Demouchy, S., Tommasi, A., Barou, F., Mainprice, D. & Cordier, P. Deformation of olivine in torsion under hydrous conditions. *Phys. Earth Planet. Inter.* **202–203,** 56–70 (2012).
61. Demouchy, S., Tommasi, A., Boffa-Ballaran, T. & Cordier, P. Low strength of Earth's uppermost mantle inferred from tri-axial deformation experiments on dry olivine crystals. *Phys. Earth Planet. Inter.* **220,** 37–49 (2013).
62. Crameri, F. & Tackley, P. J. Parameters controlling dynamically self-consistent plate tectonics and single-sided subduction in global models of mantle convection. *J. Geophys. Res.* **120,** 3680–3706 (2015).
63. Korenaga, J. Thermal cracking and the deep hydration of oceanic lithosphere: a key to the generation of plate tectonics? *J. Geophys. Res.* **112,** B05408 (2007).
64. Montesi, G. J. Fabric development as the key for forming ductile shear zones and enabling plate tectonics. *J. Struct. Geol.* **50,** 254–266 (2013).
65. Brace, W. F. & Kohlstedt, D. L. Limits on lithospheric stress imposed by laboratory experiments. *J. Geophys. Res.* **85,** 6248–6252 (1980).
66. Li, Z.-H. & Ribe, N. M. Dynamics of free subduction from 3-D boundary element modeling. *J. Geophys. Res.* **117,** B06408 (2012).
67. Govers, R. & Wortel, M. J. R. Lithosphere tearing at STEP faults: response to edges of subduction zones. *Earth Planet. Sci. Lett.* **236,** 505–523 (2005).
68. Hale, A. J. *et al*. Dynamics of slab tear faults: insights from numerical modelling. *Tectonophysics* **483,** 58–70 (2010).
69. Nijholt, N. & Govers, R. The role of passive margins on the evolution of Subduction-Transform Edge Propagators (STEPs). *J. Geophys. Res.* **120,** 7203–7230 (2015).

70. Gurnis, M., Zhong, S. & Toth, J. in *The History and Dynamics of Global Plate Motions* (eds Richards, M. A., Gordon, R. & van der Hilst, R.) 73–94 (AGU Geophysical Monograph 21, 2000).
71. Telford, W. M., Geldart, L. P., Sheriff, R. E. & Keys, D. A. *Applied Geophysics* 43 (Cambridge Univ. Press, 1976).
72. Wieczorek, M. A. *Treatise on Geophysics* Vol. 10, 165–206 (Elsevier, 2007).
73. Audet, P. Directional wavelet analysis on the sphere: application to gravity and topography of the terrestrial planets. *J. Geophys. Res.* **116,** E01003 (2011).
74. James, P. B., Zuber, M. T. & Phillips, R. J. Crustal thickness and support of topography on Venus. *J. Geophys. Res.* **118,** 859–875 (2013).